

Quantum Number Constraints from Shell Structure Govern Short-range Nucleon Pairing

D Nguyen^{1,6†}, C. Yero^{2,7†}, H. Szumila-Vance^{1,8}, F. Hauenstein¹, N. Swan²,
L.B. Weinstein^{2*}, G.A. Miller⁹, A. Schmidt³, E. Piaseckiy⁴, O. Hen⁵

¹Thomas Jefferson National Accelerator Facility, Newport News, Virginia 23606, USA

²Old Dominion University, Norfolk, Virginia 23529, USA

³The George Washington University, Washington DC 20052, USA

⁴School of Physics and Astronomy, Tel Aviv University, Tel Aviv 69978, Israel

⁵Massachusetts Institute of Technology, Cambridge, Massachusetts 02139, USA

⁶University of Tennessee, Knoxville, TN 37919, USA

⁷Catholic University of America, Washington, DC 20064, USA

⁸Florida International University, Miami, FL 33199, USA

⁹University of Washington, Seattle, WA 98195, USA

*Corresponding author. Email: weinstein@odu.edu

†These authors contributed equally to this work.

Nucleons in atomic nuclei occasionally form short-range correlated (SRC) pairs—brief, high-density, predominantly proton-neutron, configurations that dominate the high-momentum tail of nuclear wave functions. We measured electron-induced proton knockout from ^{40}Ca , ^{48}Ca , and ^{54}Fe to investigate how shell structure affects SRC formation. Despite a 40% increase in neutron number, ^{48}Ca shows only a modest rise in SRC proton probability relative to ^{40}Ca . In contrast,

adding 30% more protons in ^{54}Fe leads to a 50% increase. These trends are inconsistent with models based on mass or density, but are well described by calculations that impose angular momentum constraints on pairing nucleons. Thus quantum number compatibility, not just proximity, governs SRC formation—highlighting the interplay between long-range mean-field structure and short-range nuclear dynamics.

Atomic nuclei are complex many-body systems, often approximated as nucleons moving independently within shell-model orbitals. Yet, a substantial fraction—about 20%—form short-range correlated (SRC) pairs (*1*): tightly-bound, predominantly neutron–proton pairs with high relative momentum and large local density. These pairs dominate the high-momentum tail of the nuclear momentum distribution and carry much of the nucleons’ kinetic energy (*1–9*).

Understanding SRC formation is crucial for describing the short-range structure of nuclei and for modeling systems with densities exceeding nuclear saturation, such as neutron stars (*10, 11*). While SRC pairs have been studied across a range of nuclei, the specific factors influencing their abundance, particularly the role of nuclear shell structure, remain uncertain.

We explored this question by measuring the electron-induced knockout of high-momentum protons from ^{40}Ca , ^{48}Ca , and ^{54}Fe . These isotopes offer a controlled test: ^{40}Ca and ^{48}Ca are both doubly magic (closed shell), with the latter containing eight additional neutrons in the $1f_{7/2}$ shell. Comparing these isotopes allows us to probe whether excess neutrons in outer shells participate in SRCs with protons in inner shells. Surprisingly, we find almost no enhancement in SRC protons in ^{48}Ca . However, when six $1f_{7/2}$ protons are added to ^{48}Ca to form ^{54}Fe , we observe a $\sim 50\%$ increase in SRC pair probability.

These results challenge the expectation that SRC formation scales simply with neutron excess (*4*). Instead, they suggest that nucleons preferentially form SRC pairs with partners occupying the same shell, where spatial overlap and angular momentum alignment are maximal. These findings are consistent with a theoretical model that incorporates shell-selective pairing constraints and provides a more nuanced picture of nucleon interactions in dense matter.

Background

Electron scattering experiments have provided essential insights into short-range correlated nucleon pairs—brief, high-density configurations that dominate the high-momentum tail of nuclear wave functions. Inclusive $A(e, e')$ cross-section ratios, measured relative to deuterium at large momentum transfer ($Q^2 \geq 1.5 \text{ GeV}^2$) and large Bjorken- x ($1.5 \leq x_B = Q^2/2m\omega \leq 2$, where m is the nucleon mass and ω is the energy transfer), have established that SRCs are a universal feature of nuclei, with relative abundances that increase with nuclear mass A and become constant at large A (12–15). However, because inclusive measurements sum over all final states, they do not identify which nucleons participate in the correlations. This limits their ability to constrain the structure and dynamics of SRC pairs (16).

By also detecting the knocked nucleon, $A(e, e'p)$ and $A(e, e'n)$ experiments have refined this picture by selecting individual nucleons knocked out from SRC pairs. Duer *et al.* (4) measured the missing-momentum distributions of protons and neutrons in several nuclei (C, Al, Fe, Pb), finding that the neutron-to-proton ratio among SRC nucleons remains constant across nuclei with different neutron-to-proton ratios (N/Z). While the ratio of SRC-to-mean-field protons increased with N/Z , the corresponding ratio for neutrons remained flat. These findings support a model in which excess neutrons in asymmetric nuclei preferentially form np SRC pairs, increasing the number of high-momentum protons while keeping the SRC n/p ratio constant.

An alternative interpretation attributes the observed trends to increasing mass number (A), since both N/Z and A grow together in the measured nuclei. This ambiguity highlights the need for precision studies in systems like ^{40}Ca , ^{48}Ca , and ^{54}Fe , where shell structure and asymmetry can be independently varied.

The measured inclusive cross-section ratio of ^{48}Ca to ^{40}Ca is 1.165(14) (17), implying that adding 40% more neutrons only modestly increases the likelihood of forming SRC pairs. Since proton-proton (pp) pairs (and hence by symmetry neutron-neutron (nn) pairs) are only 5% of the SRC pairs (9) this shows that adding 40% more neutrons increased the number of np pairs by only 17%.

On the theoretical side, significant progress has been made in describing SRCs from first principles. Per-nucleon $A(e, e')$ cross-section ratios across a wide range of nuclei appear to be

independent of both the nuclear interaction and the resolution scale (18, 19), suggesting a form of scale and scheme independence. Quantum Monte Carlo calculations extended this insight by showing that the nuclear wave function factorizes at short distances into a strongly correlated pair and a residual nucleus (20). In this framework, the ratio of “contacts” (i.e., pair probabilities) between nucleus A and deuterium remains constant for very different nucleon-nucleon (NN) potentials, implying that SRC abundances are governed by mean-field quantities rather than short-range details of the nuclear force. However, such calculations remain computationally demanding for medium-to-heavy nuclei such as calcium and iron.

Phenomenological models based on the shell structure of nuclei offer additional guidance. Colle *et al.* (21) used shell-model wave functions to estimate the relative numbers of pp and pn pairs across nuclei from carbon to lead. They found that simple combinatorial models greatly over-predict SRC pairs in heavier systems, whereas more restrictive models—e.g., allowing only node-less ($n = 0$) S-state ($l = 0$) np pairs—better matched the data. A zero-range approximation (ZRA), which considers only pairs at zero relative separation, produced even better agreement, suggesting that SRCs arise from universal correlation operators acting on a small subset of nucleon pairs.

For calcium and iron isotopes specifically, Tropiano *et al.* (22) computed SRC-sensitive momentum distributions using similarity renormalization group (SRG)-evolved operators and empirically tuned single-particle wave functions. They extracted the relative fractions of high-momentum nucleons. This should approximately equal the relative SRC abundances, thus providing a theoretical benchmark for our measurements.

To complement these efforts, we developed a spatial overlap model based on measured proton charge radii (23) and calculated neutron distributions (24). The model estimates the number of proton–neutron pairs separated by less than 1 fm, and accounts for the probability that a struck proton escapes the nucleus without rescattering, using a Glauber approximation. This provides a semi-empirical prediction for SRC pair probabilities in calcium and iron.

Finally, we also introduced a more selective quantum-pairing model, requiring SRC pairs to have both zero relative ($l = 0$) and total ($L = 0$) angular momentum (25). This eliminates pairing between nucleons in different shells and leads to the concrete predictions presented here: no enhancement in SRCs for ^{48}Ca relative to ^{40}Ca , and a $\sim 30\%$ increase for ^{54}Fe due to the additional $f_{7/2}$ protons.

After accounting for different proton-rescattering effects from the different shells, the predicted $^{54}\text{Fe}/^{40}\text{Ca}$ SRC ratio rises to 1.43, within 10% of our experimental findings presented below.

Results

We measured the probability of proton knockout from SRC nucleon pairs by scattering 10.5-GeV electrons from ^{40}Ca , ^{48}Ca , and ^{54}Fe targets in Jefferson Lab's Hall C. The experiment, conducted in 2023, used the Super High Momentum Spectrometer (SHMS) (26) to detect scattered electrons and the High Momentum Spectrometer (HMS) (27) to detect recoil protons (Fig. 1). These small-aperture magnetic spectrometers determine particle momentum by tracking curvature in the magnetic field.

Our choice of nuclei was designed to isolate the effect of shell structure on SRC formation: ^{40}Ca is a doubly magic nucleus with closed proton and neutron shells. ^{48}Ca includes eight additional neutrons filling the $1f_{7/2}$ orbital, while ^{54}Fe adds six protons to the same shell (Fig. 3, inset). These variations allow us to probe how the spatial overlap and shell occupancy of nucleons influence the likelihood of forming short-range pairs.

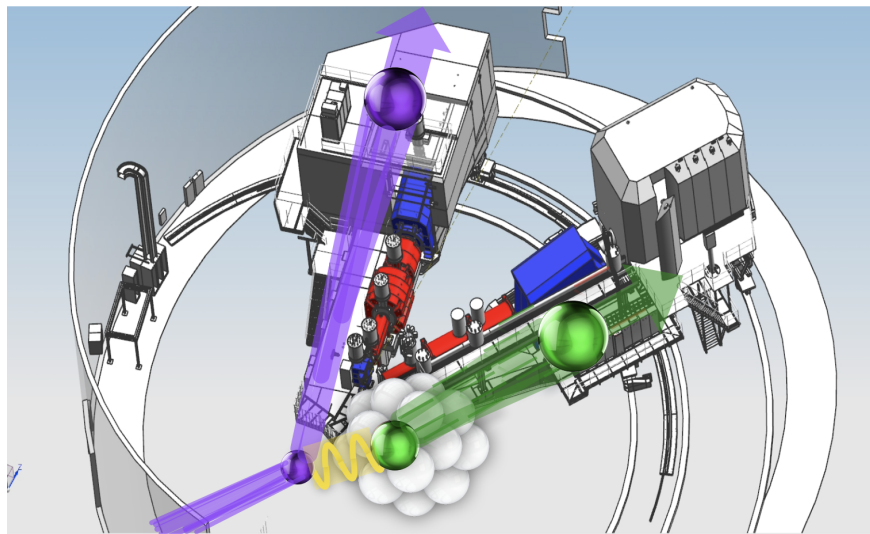


Figure 1: The layout of Jefferson Lab Hall C showing the incoming electron in purple, the scattered electron in purple as detected by the SHMS spectrometer, and the knocked-out proton in green detected in the HMS spectrometer

To select events dominated by proton knockout from SRC pairs, we required a squared momen-

tum transfer $Q^2 \geq 1.8 \text{ GeV}^2$, Bjorken scaling variable $x = Q^2/2m\omega \geq 1.2$ (where ω is the energy transfer and m is the nucleon mass), and missing momentum $0.375 \leq p_{miss} \leq 0.700 \text{ GeV}/c$. These kinematic cuts isolate quasielastic scattering from high-initial-momentum nucleons, which are predominantly members of SRC pairs (8). The missing momentum, $p_{miss} = |\vec{p} - \vec{q}|$, was calculated from the difference between the measured recoil proton momentum and the momentum transfer.

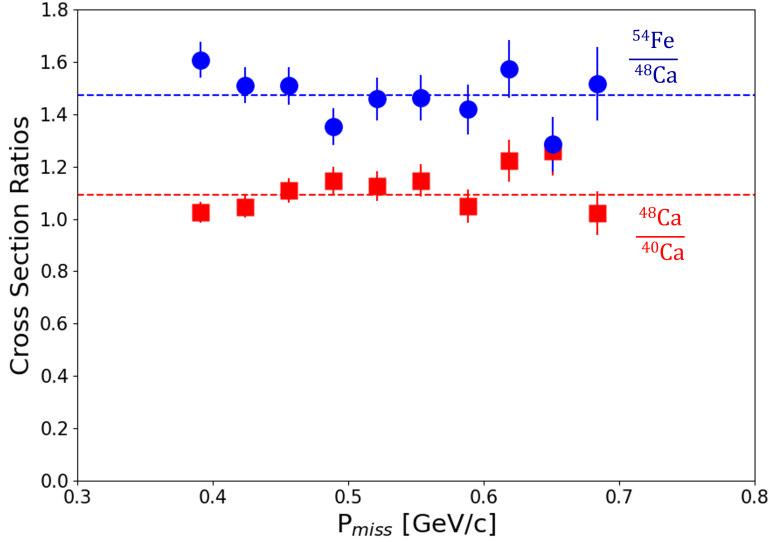


Figure 2: The per-nucleus integrated ($e, e'p$) cross-section ratios for (red squares) $^{48}\text{Ca}/^{40}\text{Ca}$ and (blue circles) $^{54}\text{Fe}/^{48}\text{Ca}$ plotted versus missing momentum p_{miss} . The dashed lines show the one-parameter fit to the data points (i.e., the weighted averages). The corresponding χ^2/dof of the fits are 1.46 ($^{48}\text{Ca}/^{40}\text{Ca}$) and 1.32 ($^{54}\text{Fe}/^{48}\text{Ca}$)

We extracted cross sections as a function of p_{miss} for each nucleus, integrated over the detector acceptances. From these, we computed cross-section ratios, which provide a relative measure of SRC-pair probabilities. The ratios of ^{48}Ca to ^{40}Ca and ^{54}Fe to ^{48}Ca are constant across the p_{miss} range (Fig. 2), as expected for proton knockout from SRC pairs.

We then averaged the per-nucleus cross-section ratios over p_{miss} (Fig. 3). We find that the SRC proton knockout rate in ^{48}Ca is 1.10 ± 0.02 times that of ^{40}Ca . This is slightly lower than, though consistent within uncertainties, with the measured inclusive ratio of 1.165 ± 0.014 (17). In contrast, the ratio of ^{54}Fe to ^{48}Ca is much larger, 1.49 ± 0.03 , indicating a substantially higher probability of

SRC proton knockout in ^{54}Fe .

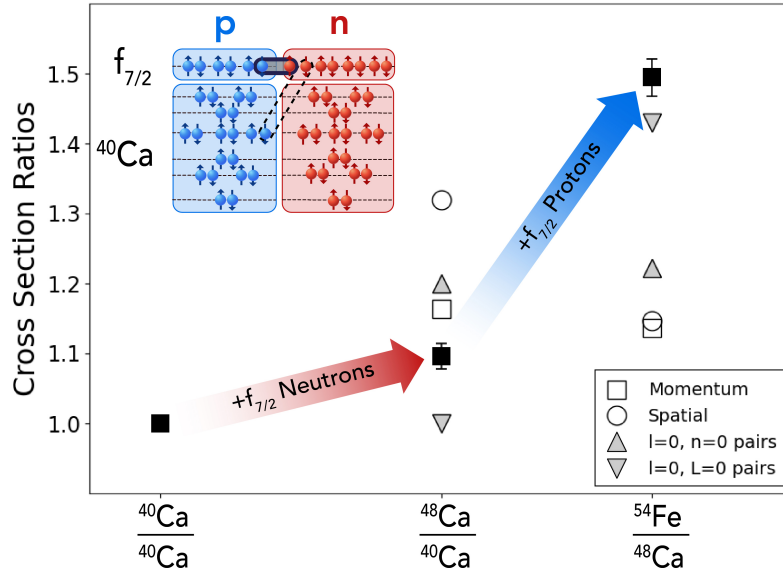


Figure 3: The per-nucleus integrated ($e, e'p$) cross-section ratios for $^{40}\text{Ca}/^{40}\text{Ca}$, $^{48}\text{Ca}/^{40}\text{Ca}$, and $^{54}\text{Fe}/^{48}\text{Ca}$ plotted versus nuclear mass A . The filled black squares show the data, the open squares show a momentum-distribution model (22), the open circles show a spatial overlap model, the gray triangles show quantum pairing calculations of (upright triangles) the Colle (21) $l = 0, n = 0$ quantum-pairing model, and (inverted triangles) the more restrictive $L = 0, l = 0$ quantum-pairing model. The upper-left inset shows the shell structure of ^{40}Ca , the eight additional $f_{7/2}$ neutrons in ^{48}Ca , and the six additional $f_{7/2}$ protons in ^{54}Fe .

This pattern reveals a striking asymmetry. Increasing the neutron number by 40% from ^{40}Ca to ^{48}Ca leads to only a $\sim 10\%$ rise in SRC proton probability. However, adding 30% more protons from ^{48}Ca to ^{54}Fe results in a $\sim 50\%$ increase. These findings suggest that the eight $f_{7/2}$ neutrons added in ^{48}Ca do not efficiently form SRC pairs with inner-shell protons. In contrast, the six $f_{7/2}$ protons added in ^{54}Fe pair strongly with the $f_{7/2}$ neutrons, likely due to increased spatial overlap and favorable quantum numbers.

A schematic summary of the inferred intra- and inter-shell pairing strengths is shown in the Fig. 3 inset. These results underscore the importance of shell structure in driving SRC formation and provide new experimental constraints for models of dense nuclear matter.

Discussion

Our results point to a key organizing principle in the formation of SRC nucleon pairs: quantum number constraints imposed by shell structure play a defining role. Models based on spatial proximity or momentum distributions fail to describe the observed ratios. Instead, models that incorporate quantum-mechanical selection rules, specifically constraints on the angular momentum states of pairing nucleons, more accurately describe the data.

Calculations by Colle et al. (21), which restrict SRC formation to neutron–proton pairs in a nodeless S -state (zero relative angular momentum, $l = 0$), overestimate the increase in SRC probability from ^{40}Ca to ^{48}Ca and underestimate the enhancement from ^{48}Ca to ^{54}Fe . A more restrictive model by Miller, which requires both zero relative ($l = 0$) and zero total ($L = 0$) angular momentum, effectively limiting pairing to nucleons in the same orbital, captures both the small change from ^{40}Ca to ^{48}Ca and the large increase from ^{48}Ca to ^{54}Fe , though it slightly underpredicts both ratios.

Together, these comparisons support a picture in which SRC pairing is governed not simply by local density or mass number, but by orbital alignment and angular momentum compatibility between nucleons. In ^{48}Ca , the added neutrons occupy the $1f_{7/2}$ orbital, which appears poorly matched for pairing with inner-shell protons. In contrast, the additional $f_{7/2}$ protons in ^{54}Fe share the same orbital as the excess neutrons, enabling a substantial increase in pairing probability—consistent with a strong intra-shell pairing preference.

These findings impose important new constraints on theoretical models of nuclear structure and the dynamics of dense nuclear matter. They suggest that SRC formation is not only a simply a universal many-body feature of the nuclear wave function, but also reflects the quantum architecture of the nucleus itself. By demonstrating that angular momentum selection rules shape the SRC landscape, this work opens new pathways for exploring the interplay between mean-field structure and short-range dynamics in nuclei—and, by extension, in neutron-rich matter such as that found in neutron stars.

Outlook

The emerging picture of SRC formation as governed by shell structure and quantum number compatibility offers a new framework for interpreting high-momentum components in nuclei. Future measurements that extend this approach across wider isotopic chains and heavier elements could test the universality of these constraints and further disentangle the role of orbital geometry. For example, measurements of SRC pairs in oxygen isotopes could test intra- and inter-shell pairing. On the theoretical front, incorporating angular momentum selection rules into ab-initio calculations and effective field theories may yield improved predictions for the SRC landscape across the nuclear chart. These insights are also essential for modeling the structure of neutron-rich matter in extreme environments, including neutron stars, where SRCs influence the equation of state, neutrino opacities, and dense-matter response. Ultimately, bridging mean-field structure and short-range dynamics is key to a unified description of nuclear matter from finite nuclei to astrophysical scales.

References and Notes

1. O. Hen, G. A. Miller, E. Piasezky, L. B. Weinstein, Nucleon-Nucleon Correlations, Short-lived Excitations, and the Quarks Within. *Rev. Mod. Phys.* **89** (4), 045002 (2017), doi:10.1103/RevModPhys.89.045002.
2. E. I. Piasezky, L. B. Weinstein, *Measurements of NN Correlations in Nuclei* (Springer Singapore), pp. 1–22 (2022), doi:10.1007/978-981-15-8818-1_60-1.
3. A. Schmidt, *et al.*, Probing the core of the strong nuclear interaction. *Nature* **578** (7796), 540–544 (2020), doi:10.1038/s41586-020-2021-6.
4. M. Duer, *et al.*, Probing high-momentum protons and neutrons in neutron-rich nuclei. *Nature* **560** (7720), 617–621 (2018), doi:10.1038/s41586-018-0400-z.
5. E. O. Cohen, *et al.*, Center of Mass Motion of Short-Range Correlated Nucleon Pairs studied via the $A(e, e'pp)$ Reaction. *Phys. Rev. Lett.* **121** (9), 092501 (2018), doi:10.1103/PhysRevLett.121.092501.
6. M. Duer, *et al.*, Direct Observation of Proton-Neutron Short-Range Correlation Dominance in Heavy Nuclei. *Phys. Rev. Lett.* **122**, 172502 (2019), doi:10.1103/PhysRevLett.122.172502.
7. I. Korover, *et al.*, $^{12}\text{C}(e, e'pN)$ measurements of short range correlations in the tensor-to-scalar interaction transition region. *Phys. Lett. B* **820**, 136523 (2021), doi:10.1016/j.physletb.2021.136523.
8. I. Korover, *et al.*, Observation of large missing-momentum $(e, e'p)$ cross-section scaling and the onset of correlated-pair dominance in nuclei. *Phys. Rev. C* **107** (6), L061301 (2023), doi:10.1103/PhysRevC.107.L061301.
9. R. Subedi, *et al.*, Probing Cold Dense Nuclear Matter. *Science* **320**, 1476–1478 (2008), doi:10.1126/science.1156675.
10. B.-A. Li, B.-J. Cai, L.-W. Chen, J. Xu, Nucleon effective masses in neutron-rich matter. *Progress in Particle and Nuclear Physics* **99**, 29–119 (2018).

11. O. Hen, B.-A. Li, W.-J. Guo, L. B. Weinstein, E. Piassetzky, Symmetry energy of nucleonic matter with tensor correlations. *Phys. Rev. C* **91**, 025803 (2015), doi:10.1103/PhysRevC.91.025803.
12. K. Egiyan, *et al.* *Phys. Rev. C* **68**, 014313 (2003).
13. K. Egiyan, *et al.*, Measurement of 2- and 3-nucleon short range correlation probabilities in nuclei. *Phys. Rev. Lett.* **96**, 082501 (2006).
14. N. Fomin, *et al.*, New measurements of high-momentum nucleons and short-range structures in nuclei. *Phys. Rev. Lett.* **108**, 092502 (2012).
15. B. Schmookler, *et al.*, Modified structure of protons and neutrons in correlated pairs. *Nature* **566** (7744), 354–358 (2019), doi:10.1038/s41586-019-0925-9.
16. R. Weiss, *et al.*, Extracting the number of short-range correlated nucleon pairs from inclusive electron scattering data. *Phys. Rev. C* **103** (3), L031301 (2021), doi:10.1103/PhysRevC.103.L031301.
17. D. Nguyen, *et al.*, Novel observation of isospin structure of short-range correlations in calcium isotopes. *Phys. Rev. C* **102**, 064004 (2020), doi:10.1103/PhysRevC.102.064004, <https://link.aps.org/doi/10.1103/PhysRevC.102.064004>.
18. J.-W. Chen, W. Detmold, J. E. Lynn, A. Schwenk, Short Range Correlations and the EMC Effect in Effective Field Theory. *Phys. Rev. Lett.* **119** (26), 262502 (2017), doi:10.1103/PhysRevLett.119.262502.
19. J. Lynn, *et al.*, Ab initio short-range-correlation scaling factors from light to medium-mass nuclei. *J. Phys. G* **47** (4), 045109 (2020), doi:10.1088/1361-6471/ab6af7.
20. R. Cruz-Torres, *et al.*, Many-Body Factorization and Position-Momentum Equivalence of Nuclear Short-Range Correlations. *Nature Physics* **17**, 306 (2020).
21. C. Colle, *et al.*, Extracting the mass dependence and quantum numbers of short-range correlated pairs from $A(e, e' p)$ and $A(e, e' pp)$ scattering. *Phys. Rev. C* **92**, 024604 (2015), doi:10.1103/PhysRevC.92.024604.

22. A. J. Tropiano, *et al.*, High-resolution momentum distributions from low-resolution wave functions. *Phys. Lett. B* **852**, 138591 (2024), doi:10.1016/j.physletb.2024.138591.
23. H. De Vries, C. W. De Jager, C. De Vries, Nuclear charge and magnetization density distribution parameters from elastic electron scattering. *Atom. Data Nucl. Data Tabl.* **36**, 495–536 (1987), doi:10.1016/0092-640X(87)90013-1.
24. S. J. Novario, D. Lonardonì, S. Gandolfi, G. Hagen, Trends of Neutron Skins and Radii of Mirror Nuclei from First Principles. *Phys. Rev. Lett.* **130** (3), 032501 (2023), doi:10.1103/PhysRevLett.130.032501.
25. A. Lane, *Nuclear Theory* (W.A. Benjamin, New York) (1964).
26. S. Ali, *et al.*, The SHMS 11 GeV/c Spectrometer in Hall C at Jefferson Lab (2025).
27. O. K. Baker, *et al.*, The High Momentum Spectrometer drift chambers in Hall C at CEBAF. *Nucl. Instrum. Meth. A* **367**, 92–95 (1995), doi:10.1016/0168-9002(95)00737-7.
28. D. Bhetuwal, *et al.*, Constraints on the onset of color transparency from quasielastic C12(e,e'p) up to Q²=14.2(GeV/c)². *Phys. Rev. C* **108** (2), 025203 (2023), doi:10.1103/PhysRevC.108.025203.
29. M. Sargsian, Private communication.
30. C. Yero, *et al.*, Probing the Deuteron at Very Large Internal Momenta. *Phys. Rev. Lett.* **125** (26), 262501 (2020), doi:10.1103/PhysRevLett.125.262501.
31. D. Dutta, K. Hafidi, M. Strikman, Color Transparency: past, present and future. *Prog. Part. Nucl. Phys.* **69**, 1–27 (2013), doi:10.1016/j.pnpnp.2012.11.001.
32. O. Hen, *et al.*, Momentum sharing in imbalanced Fermi systems. *Science* **346**, 614–617 (2014), doi:10.1126/science.1256785.
33. M. Duer, *et al.*, Measurement of Nuclear Transparency Ratios for Protons and Neutrons. *Phys. Lett.* **B797**, 134792 (2019), doi:10.1016/j.physletb.2019.07.039.

Acknowledgments

We acknowledge the efforts of the staff of the Accelerator and Physics Divisions at Jefferson Lab that made this experiment possible. ... We acknowledge support from ... and the United States-Israel Binational Science Foundation (BSF) grant 2018093. Jefferson Science Associates operates the Thomas Jefferson National Accelerator Facility for the DOE, Office of Science, Office of Nuclear Physics under contract DE-AC05-06OR23177.

Supplementary materials

Materials and Methods

Supplementary Text

Table S1 References (7-33)

Supplementary Materials for

Quantum Number Constraints from Shell Structure Govern

Short-range Nucleon Pairing

D Nguyen[†], C. Yero[†], H. Szumila-Vance, F. Hauenstein, N. Swan,
L.B. Weinstein^{*}, G.A. Miller, A. Schmidt, E. Piasezky, O. Hen

^{*}Corresponding author. Email: example@mail.com

[†]These authors contributed equally to this work.

This PDF file includes:

Materials and Methods

Supplementary Text

Table S1

Materials and Methods

Table S1: Targets

Target	Areal Thickness (g/cm ²)	Purity
⁴⁰ Ca	0.800	100%
⁴⁸ Ca	1.050	90%
⁵⁴ Fe	0.415	98%

The measurement described in this paper was carried out in 2022-2023 using the facilities of Hall C of the Thomas Jefferson National Accelerator Facility (Jefferson Lab) in Newport News, Virginia. We scattered a 30–60 μA , 10.5-GeV electron beam from ⁴⁰Ca, ⁴⁸Ca, and ⁵⁴Fe targets. We detected the scattered electrons in the SHMS spectrometer (28), which has a nominal solid angle of ≈ 4.0 msr with a fractional momentum acceptance of $-10\% \leq \frac{\Delta p}{p_0} \leq 22\%$. We used a pair of horizontal drift chambers for tracking, two pairs of $x - y$ scintillator hodoscope planes for triggering and timing, and a lead-glass calorimeter for electron identification. The SHMS was set to a central momentum $p_0 = 8.55$ GeV/c and a central angle of $\theta_e = 8.3^\circ$.

We detected the knocked-out protons in the HMS spectrometer (28), which has a nominal solid angle of 6 msr and an 18% momentum acceptance. We used a pair of horizontal drift chambers for tracking, and two pairs of $x - y$ scintillator hodoscope planes for triggering and timing. The HMS central momentum was $p_0 = 1.325$ GeV/c and the central angle was $\theta_p = 66.4^\circ$ for data taking. The missing momentum and energy are $\vec{p}_{miss} = \vec{p}_p - \vec{q}$ and $E_{miss} = \omega - T_p$ where \vec{p}_p and T_p are the three-momentum and kinetic energy of the detected proton, respectively.

We traced the electron and the proton back to the interaction vertex and determined their time difference. Out-of-time events were sampled and subtracted from the coincidence peak.

We measured elastic electron scattering from hydrogen, $\text{H}(e, e')$ and $\text{H}(e, e'p)$, for calibrations and normalization. We calibrated the momentum of the SHMS by varying the magnetic field to vary p_0 and thus scan the location of the hydrogen elastic peak across the SHMS focal plane. We determined the overall normalization and checked that the spectrometers were performing well by comparing the measured $\text{H}(e, e')$ and $\text{H}(e, e'p)$ cross sections to the world data. This normalization

canceled in the cross-section ratios. We determined the tracking efficiency in each spectrometer by selecting events with good particle hits in the central parts of the scintillator hodoscopes and determining the fraction of events with good tracks in the drift chambers. Electronic deadtime correction factors were measured in each spectrometer with a dedicated random trigger.

is anything missing?

Both Ca targets were coated with a thin layer of light mineral oil (typically $(\text{CH}_2)_n$) to prevent oxidation. We measured the target oil contamination in two ways. First, we measured the peak at $E_{miss} = 0$ and $p_{miss} = 0$ for $\text{Ca}(e, e'p)$ calibration runs to measure the H contamination. Second, we used the rate of SHMS single-arm electron triggers per incident electron for $\text{Ca}(e, e')$ to measure the total target plus oil contamination in each run. The ^{48}Ca oil contamination decreased exponentially from about 3% to about 0.5% during the data taking as the oil evaporated. The ^{40}Ca contamination was constant at about 0.5%. These total oil contamination values were consistent with the measured H contamination for $(\text{CH}_2)_n$ mineral oil. We subtracted the contamination using our measured $\text{C}(e, e'p)$ data.

We also used the measured ^{40}Ca data to subtract the 10% ^{40}Ca contamination from our 90%-pure ^{48}Ca target data. We did not correct the ^{54}Fe data for the 2% ^{56}Fe contamination.

To select SRC events we required that all events have momentum transfer $Q^2 \geq 1.8 \text{ GeV}^2$, $x \geq 1.2$ and $0.375 \leq p_{miss} \leq 0.700 \text{ GeV}/c$. The Q^2 and x cuts select quasielastic scattering events, where the electron scatters elastically from a single bound nucleon. The $p_{miss} = 0.375 \text{ GeV}/c$ lower limit corresponds approximately to the onset of NN SRC pair dominance (8).

The outgoing proton can rescatter in the residual nucleus (final state interactions or FSI), shifting p_{miss} to larger values and contaminating the SRC sample. Most of these collisions deflect the outgoing proton slightly, leading to a peak at $\theta_{rq} \approx 70^\circ$, where θ_{rq} is the angle between the recoil momentum $\vec{p}_r = -\vec{p}_{miss} = \vec{q} - \vec{p}_p$ and the three-momentum transfer \vec{q} (29). This same effect can be seen in proton knockout from deuterium (30). We therefore required $\theta_{rq} \leq 40^\circ$ for the SRC events to reduce the effects of FSI.

We calculated the depletion of the outgoing protons due to rescattering out of our experimental acceptance (31) using a Glauber calculation (32) and calculated the uncertainty by comparing these transparency ratios with those from a Glauber calculation with different parameters and using $T \propto A^{-0.289}$ (33). The transparency factor ratios used were $T_{48/40} = 0.910 \pm 0.013$ and

$$T_{54/48} = 0.967 \pm 0.013.$$

For each target nucleus A we converted the number of detected events to a cross section:

$$\sigma = \frac{N}{Qt\epsilon T_A R_A}$$

where N is the number of events for nucleus A , Q is the integrated number of incident electrons, t is the areal target thickness in nuclei/cm² calculated from Table S1, $\epsilon = \epsilon_{HMS}^T \epsilon_{SHMS}^T \epsilon_{LT} \epsilon_{EDT} \epsilon_{HMS}^P$ is an efficiency correction that includes the HMS and SHMS tracking efficiencies, the electronic dead time, the computer live time, and the HMS proton detection efficiency, T_A is the nuclear transparency for nucleus A , and R_A is the radiative correction factor.

R_A is determined from the ratio of the radiated to unradiated plane-wave impulse approximation cross sections calculated using the Benhar spectral functions for C, ⁵⁶Fe, and Au and the Hall C “SIMC” event generator and spectrometer simulator integrated over our experimental kinematics. Because R_A varied very slowly from C to Au, we used the same radiative correction factor for ⁴⁰Ca, ⁴⁸Ca, and ⁵⁴Fe, and assigned a systematic uncertainty in the ratio of 1%.

We integrated the number of events over the experimental acceptances for each nucleus and calculated the ⁴⁸Ca to ⁴⁰Ca and ⁵⁴Fe to ⁴⁸Ca ratios.

The systematic uncertainties include contributions from radiative and transparency corrections, and from cut variations. For each cut, we determined the 1σ “reasonable” cut variation. We then varied all the cuts simultaneously, randomly selecting the value of each cut from a gaussian distribution and calculating the cross section ratios for each set of cuts. The uncertainty in the cross section ratio is the standard deviation of the resulting ratio distribution. The cut variation uncertainties were 1% for both the ⁴⁸Ca/⁴⁰Ca and the ⁵⁴Fe/⁴⁸Ca ratios. Due to taking ratios of similar nuclei, the systematic uncertainties in the ratios were small.